

Dark matter in early-type spiral galaxies: the case of NGC 2179 and of NGC 2775^{*,**}

E.M. Corsini¹, A. Pizzella², M. Sarzi³, P. Cinzano³, J.C. Vega Beltrán⁴, J.G. Funes S.J.³, F. Bertola³, M. Persic⁵, and P. Salucci⁶

¹ Osservatorio Astrofisico di Asiago, Dipartimento di Astronomia, Università di Padova, via dell'Osservatorio 8, I-36012 Asiago, Italy

² European Southern Observatory, Alonso de Cordova 3107, Casilla 19001, Santiago 19, Chile

³ Dipartimento di Astronomia, Università di Padova, vicolo dell'Osservatorio 5, I-35122 Padova, Italy

⁴ Osservatorio Astronomico di Padova, Telescopio Nazionale Galileo, vicolo dell'Osservatorio 5, I-35122 Padova, Italy

⁵ Osservatorio Astronomico di Trieste, via G.B. Tiepolo 11, I-34131 Trieste, Italy

⁶ SISSA, via Beirut 2–4, I-34013 Trieste, Italy

Received 8 June 1998 / Accepted 3 November 1998

Abstract. We present the stellar and ionized-gas velocity curves and velocity-dispersion profiles along the major axis for six early-type spiral galaxies.

Two of these galaxies, namely NGC 2179 and NGC 2775, are particularly suited for the study of dark matter halos. Using their luminosity profiles and modeling their stellar and gaseous kinematics, we derive the mass contributions of the luminous and the dark matter to the total potential. In NGC 2179 we find that the data (measured out to about the optical radius R_{opt}) unambiguously require the presence of a massive dark halo. For the brighter and bigger object NGC 2775, we can rule out a significant halo contribution at radii $R \lesssim 0.6 R_{\text{opt}}$. Although preliminary, these results agree with the familiar mass distribution trend known for late-type spirals of comparable mass.

Key words: galaxies: individual: NGC 2179 – galaxies: individual: NGC 2775 – galaxies: kinematics and dynamics – galaxies: spiral – cosmology: dark matter

1. Introduction

Recent analyses of extended rotation curves (RCs) of late-type spiral galaxies (Persic, Salucci & Stel 1996) have confirmed that in spirals of all luminosities a substantial dark matter (DM) component is detectable already in the optical region. The effect is stronger at lower luminosities: the dark-to-visible mass ratio at the optical radius R_{opt} ¹ scales with luminosity $\propto L^{-0.7}$.

Send offprint requests to: E.M. Corsini

* Based on observations carried out at ESO, La Silla (Chile) (ESO N. 52, 1-020) and on observations obtained with the VATT: the Alice P. Lennon Telescope and the Thomas J. Bannan Astrophysics Facility.

** Tables 4 to 42 are only available in electronic form at the CDS via anonymous ftp to cdsarc.u-strasbg.fr (130.79.128.5) or via <http://cdsweb.u-strasbg.fr/Abstract.html>.

Correspondence to: (corsini@pd.astro.it)

¹ $R_{\text{opt}} = 3.2 R_D$ is the radius encompassing the 83% of the total integrated light. R_D is the scale-length of the exponential surface

For early-type spirals the status of our knowledge is different. The RCs presently available for these objects are fragmentary (in particular in the nuclear regions), and only extend to $\lesssim 2 R_D$ (see Rubin et al. 1985). Consequently, detailed mass decomposition have so far not been possible for these systems. In particular, it is not known whether dark halos are unambiguously present also in early-type spirals.

It may be conjectured that for a given $V(R_{\text{opt}})$ the DM fraction within the optical size is smaller in early than in late-type spirals: this, because in an early spiral the conspicuous stellar bulge, with $(M/L)_{\text{bulge}} \gtrsim 3(M/L)_{\text{disk}}$, can supply a mass compact enough to make the rotation velocity higher than (see Rubin et al. 1985), and the velocity profile different from, that of a late spiral of similar luminosity. In this case, the derivation of the halo parameters would be more uncertain for early than for late types: in fact, at small radii not two mass components (disk + halo, like in Sc-Sd galaxies), but three mass components (bulge + disk + halo) will have locally similar (solid-body like) behaviors. So for non-extended RC data the mass solution of an Sa galaxy would be degenerate even within the maximum-disk solution.

In this paper we present the velocity and velocity-dispersion profiles of the stars and the ionized gas, measured along the major axis, for six early-type spirals. The six selected galaxies (Table 1) were already known to show emission lines and their photometric properties were known. Of these, 5 had already been observed spectroscopically by Rubin et al. (1985), who obtained the RCs of the ionized gas, and photometrically by Kent (1988). NGC 2179 was the only galaxy in our sample still lacking spectroscopical and photometrical observations. To the originally observed sample belonged the early-type spiral NGC 3593 too. Its stellar and the gaseous kinematics, found to exhibit a star vs. star counterrotation, is presented and discussed by Bertola et al. (1996). Three-component models (bulge

brightness distribution $I(r) = I(0) e^{-r/R_D}$. For a Freeman (1970) disk, R_{opt} corresponds to the de Vaucouleurs 25 B -mag arcsec⁻² photometric radius.

Table 1. Parameters of the sample galaxies.

object	type		B_T	P.A.	i	V_\odot	V_0	D	scale	R_{25}	$R_{\text{star}}^{\text{far}}$	$R_{\text{gas}}^{\text{far}}$	time
[name]	[RSA]	[RC3]	[mag]	[$^\circ$]	[$^\circ$]	[km s^{-1}]	[km s^{-1}]	[Mpc]	[pc''^{-1}]	[$''$]	[$''$]	[$''$]	[h]
(1)	(2)	(3)	(4)	(5)	(6)	(7)	(8)	(9)	(10)	(11)	(12)	(13)	(14)
NGC 2179	Sa	.SAS0..	13.22	170	51	2885 ± 10	2673	35.6	172.6	51	41	54	8.5
NGC 2775	Sa(r)	.SAR2..	11.03	163	44	1350 ± 10	1180	15.7	76.1	128	100	77	6.5
NGC 3281	Sa	.SAS2P*	12.70	138	69	3380 ± 10	3098	41.3	200.2	99	86	50	6.5
IC 724	Sa	.S..1..	13.4	60	55	5974 ± 10	5853	78.0	378.2	70	62	56	2.0
NGC 4698	Sa	.SAS2..	11.46	170	70	992 ± 10	909	12.1	58.7	119	76	113	4.7
NGC 4845	Sa	.SAS2./	12.10	75	72	1084 ± 10	980	13.1	63.5	150	87	100	4.0

Notes – Col.(2): classification from RSA (Sandage & Tamman 1981). Col.(3): classification from RC3 (de Vaucouleurs et al. 1991). Col.(4): total observed blue magnitude from RC3 except for IC 724 (RSA). Col.(5): observed position angle. Col.(6): inclination from Rubin et al. (1985) except for NGC 2179 (Tully 1988). Col.(7): heliocentric velocity of the galaxy derived as center of symmetry of the gas RC. Col.(8): systemic velocity derived from V_\odot corrected for the motion of the Sun with respect of the Local Group by $\Delta V = 300 \cos b \sin l$. Col.(9): distance obtained as V_0/H_0 with $H_0 = 75 \text{ km s}^{-1} \text{ Mpc}^{-1}$. Col.(11): radius of the 25 B -mag arcsec^{-2} isophote from RC3. Col.(12): radius of the farthest measured stellar velocity. Col.(13): radius of the farthest measured gas velocity. Col.(14): total integration time of the spectroscopic observation.

+ disk + halo) based on observed photometry and kinematics are obtained for two galaxies of the sample: NGC 2179 and NGC 2775.

2. Observations and data reduction

2.1. The spectroscopic observations

The spectroscopic observations of our sample galaxies were carried out at the ESO 1.52-m Spectroscopic Telescope at La Silla on February 15–19, 1994.

The telescope was equipped with the Boller & Chivens Spectrograph. The No. 26 grating with $1200 \text{ grooves mm}^{-1}$ was used in the first order in combination with a $2''.5 \times 4''.2$ slit. It yielded a wavelength coverage of 1990 \AA between about 5200 \AA and about 7190 \AA with a reciprocal dispersion of $64.80 \text{ \AA mm}^{-1}$. The instrumental resolution was derived measuring after calibration the FWHM of 22 individual emission lines distributed all over the spectral range in the 10 central rows of a comparison spectrum. We checked that the measured FWHM's did not depend on wavelength, and we found a FWHM mean value of 2.34 \AA . This corresponds to $\sigma = 0.99 \text{ \AA}$ (i.e., 51 km s^{-1} at 5800 \AA and 46 km s^{-1} at 6400 \AA). The adopted detector was the No. 24 2048×2048 Ford CCD, which has a $15 \times 15 \mu\text{m}^2$ pixel size. After an on-chip binning of 3 pixels along the spatial direction, each pixel of the frame corresponds to $0.97 \text{ \AA} \times 2''.43$.

The long-slit spectra of all the galaxies were taken along their optical major axes. At the beginning of each exposure the galaxy was centered on the slit using the guiding camera. Repeated exposures (typically of 3600 s each) did ensure several hours of effective integration without storing up too many cosmic rays. Some long-slit spectra of 8 late-G or early-K giant stars, obtained with the same instrumental setup, served as templates in measuring the stellar kinematics. Their spectral classes range from G8III to K4III (Hoffleit & Jaschek 1982).

The typical value of the seeing FWHM during the observing nights, measured by the La Silla Differential Image Motion

Monitor (DIMM), was $1'' - 1''.5$. Comparison helium-argon lamp exposures were taken before and after every object exposure. The logs of the spectroscopic observations of galaxies and template stars are reported in Tables 2 and 3, respectively.

2.1.1. Data reduction

Using standard MIDAS² routines, all the spectra were bias subtracted, flat-field corrected by quartz lamp exposures, and cleaned from cosmic rays. Cosmic rays were identified by comparing the counts in each pixel with the local mean and standard deviation, and then corrected by substituting a suitable value.

A small misalignment was present between the CCD and the slit. We measured a difference of $\Delta Y \simeq 1.4$ pixel between the positions of the center of the stellar continuum near the blue and red edge of the spectra. When measuring the stellar kinematics, the tilt had to be removed. This was done by rotating the spectra by a suitable angle ($\theta = 0^\circ.04$) before the wavelength calibration. We noticed however that the sharp line profile of the emission lines was spoiled by the rotating algorithm. For this reason no rotation was applied when measuring the ionized-gas kinematics.

The wavelength calibration was done using the MIDAS package XLONG. We determined the velocity error possibly introduced by the calibration measuring the ‘velocity curve’ of a sample of 24 OH night-sky emission lines distributed all over the spectral range. The velocity did not show any significant dependence on radius, indicating that the wavelength rebinning had been done properly. We found a mean deviation from the predicted wavelengths (Osterbrock et al. 1996) of 2 km s^{-1} .

After calibration, the different spectra obtained for a given galaxy were co-added using their stellar-continuum centers as reference. For each spectrum the center was assumed as the center of the Gaussian fitting the mean radial profile of the stellar

² MIDAS is developed and maintained by the European Southern Observatory.

Table 2. Log of spectroscopic observations (galaxies).

object [name] (1)	date [d m y] (2)	U.T. [h m] (3)	time [s] (4)
NGC 2179	15 Feb 1994	01 24	3600
NGC 2179	15 Feb 1994	02 32	3600
NGC 2179	16 Feb 1994	01 17	5400
NGC 2179	17 Feb 1994	01 41	3600
NGC 2179	18 Feb 1994	00 26	3600
NGC 2179	18 Feb 1994	01 35	3600
NGC 2179	19 Feb 1994	00 19	3600
NGC 2179	19 Feb 1994	01 27	3600
NGC 2775	15 Feb 1994	04 10	3600
NGC 2775	15 Feb 1994	05 17	3600
NGC 2775	16 Feb 1994	03 56	5400
NGC 2775	17 Feb 1994	02 47	3600
NGC 2775	17 Feb 1994	03 53	3600
NGC 2775	18 Feb 1994	02 41	3600
NGC 3281	16 Feb 1994	04 39	5400
NGC 3281	16 Feb 1994	06 14	3600
NGC 3281	17 Feb 1994	05 02	3600
NGC 3281	18 Feb 1994	03 50	3600
NGC 3281	19 Feb 1994	02 34	3600
NGC 3281	19 Feb 1994	03 40	3600
IC 724	17 Feb 1994	06 16	3600
IC 724	17 Feb 1994	07 21	3600
NGC 4698	16 Feb 1994	07 22	3600
NGC 4698	16 Feb 1994	08 28	3600
NGC 4698	18 Feb 1994	07 17	3600
NGC 4698	19 Feb 1994	07 42	6000
NGC 4845	15 Feb 1994	07 02	3600
NGC 4845	15 Feb 1994	08 08	3600
NGC 4845	17 Feb 1994	05 02	3600
NGC 4845	18 Feb 1994	08 25	3600

Notes – Cols.(2–3): date and time of start of exposure. Col.(4): exposure time.

continuum. The contribution of the sky was determined from the edges of the resulting galaxy frames and then subtracted.

2.1.2. Measuring the gas kinematics

The ionized-gas velocities (v_g) and velocity dispersions (σ_g) were measured by means of the MIDAS package ALICE. We measured the [N II] lines ($\lambda\lambda$ 6548.03, 6583.41 Å), the H α line (λ 6562.82 Å), and the [S II] lines ($\lambda\lambda$ 6716.47, 6730.85 Å), where they were clearly detected. The position, the FWHM, and the uncalibrated flux F of each emission line were determined by interactively fitting one Gaussian to each line plus a polynomial to its local continuum. The center wavelength of the fitting Gaussian was converted into velocity in the optical convention $v = cz$; then the standard heliocentric correction was applied. The Gaussian FWHM was corrected for the instrumental FWHM, and then converted into the velocity dispersion σ . In the regions where the intensity of the emission lines was

Table 3. Log of spectroscopic observations (template stars).

object [name] (1)	type [BSC] (2)	date [d m y] (3)	U.T. [h m] (4)	time [s] (5)
HR 2035	G8III	15 Feb 1994	00 53	2
HR 2035	G8III	17 Feb 1994	00 04	2
HR 2035	G8III	17 Feb 1994	00 07	3
HR 2035	G8III	17 Feb 1994	00 10	4
HR 2035	G8III	17 Feb 1994	00 16	3
HR 2035	G8III	19 Feb 1994	00 07	2
HR 2035	G8III	19 Feb 1994	00 09	3
HR 2429	K1III	18 Feb 1994	00 08	2
HR 2429	K1III	18 Feb 1994	00 11	2
HR 2429	K1III	18 Feb 1994	00 14	3
HR 2443	K1III	16 Feb 1994	00 25	3
HR 2503	K4III	16 Feb 1994	00 35	4
HR 2503	K4III	16 Feb 1994	00 38	4
HR 2503	K4III	16 Feb 1994	00 41	4
HR 2503	K4III	16 Feb 1994	00 46	4
HR 2503	K4III	16 Feb 1994	00 49	8
HR 3431	K4III	15 Feb 1994	03 52	4
HR 5100	K0III	19 Feb 1994	09 29	10
HR 5100	K0III	19 Feb 1994	09 32	7
HR 5196	K0.5III	16 Feb 1994	09 33	4
HR 5196	K0.5III	16 Feb 1994	09 38	15
HR 5196	K0.5III	16 Feb 1994	09 43	10
HR 5315	K3III	15 Feb 1994	09 14	4
HR 5315	K3III	15 Feb 1994	09 17	3
HR 5315	K3III	15 Feb 1994	09 21	3
HR 5601	K0.5III	15 Feb 1994	09 29	3
HR 5601	K0.5III	15 Feb 1994	09 32	4
HR 5601	K0.5III	15 Feb 1994	09 35	4
HR 5601	K0.5III	15 Feb 1994	09 39	10

Notes – Col.(2): spectral class of the template star from The Bright Star Catalogue (Hoffleit & Jaschek 1982). Cols.(3–4): date and time of start of exposure. Col.(5): exposure time.

low, we binned adjacent spectral rows in order to improve the signal-to-noise ratio, S/N , of the lines.

We expressed the variation of the r.m.s. velocity error δv as a function of the relevant line S/N ratio. In order to find the expression for $\delta v = \delta v(S/N)$, we selected the same 16 night-sky emission lines in the spectra of NGC 2775, NGC 3281, IC 724 and NGC 4845. Such night-sky emissions were chosen to have different intensities and different wavelengths between 6450 Å and 6680 Å (i.e. the wavelength range of the observed emission lines of the ionized gas) in the four spectra. We derived the sky spectra by averaging several rows along the spatial direction in a galaxy-light free region. Using the above package, we interactively fitted one Gaussian emission plus a polynomial continuum to each selected sky line and its local continuum. We derived the flux F and the FWHM of the sample lines, taking the ratio F/FWHM as the signal S . For each galaxy spectrum the noise N was defined as the r.m.s. of the counts measured in

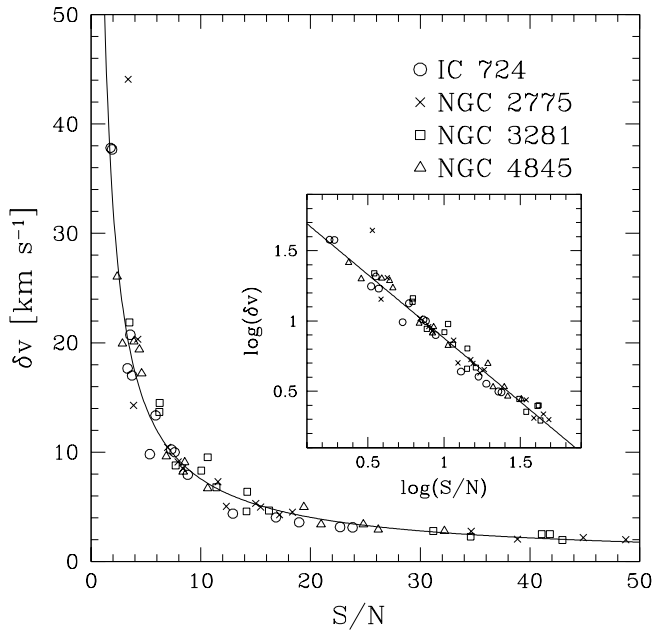


Fig. 1. The variation of the r.m.s. velocity error δv as a function of the signal-to-noise ratio S/N . The symbols (triangles, circles, squares and crosses) represent the r.m.s. δv of the quadratic polynomials fitting the ‘velocity curves’ of the same 16 night-sky emission lines selected in 4 different spectra (NGC 2775, NGC 3281, IC 724 and NGC 4845 respectively) as a function of the relevant S/N ratio of the lines. The full line represents the power law fitting the data. In the insert the data are plotted in logarithmic scale

regions of the frame where the contributions of both the galaxy and the sky lines were negligible. The resulting S/N range was large ($1 \leq S/N \leq 50$). For each sample emission line we then measured, by means of an automatic procedure, the night-sky ‘velocity curve’ along the full slit extension. The wavelengths of the emissions were evaluated with Gaussian fits and then converted to velocities. The radial profiles of the sky-line velocities were then fitted by quadratic polynomials. We assumed the r.m.s. of the fit to each ‘velocity curve’ to be the 1σ velocity error. Fig. 1 shows the good agreement between the distributions of the $(S/N, \delta v)$ measurements taken in the 4 different spectra. In log-log scale, the $(S/N, \delta v)$ relation is well represented by a straight line, that corresponds to:

$$\delta v = 60.4 \left(\frac{S}{N} \right)^{-0.90} \text{ km s}^{-1} \quad (1)$$

(least-squares fit). This result agrees with Keel’s (1996) relation $\delta v \propto (S/N)^{-1}$, based on numerical simulations. Once the relevant S/N ratio of the emission had been derived, we obtained δv for each velocity measurement of the ionized-gas component by means of Eq. 1. The gas velocities derived independently from different emission lines are in mutual agreement within their errors δv .

The ionized-gas velocities and velocity dispersions from $[\text{N II}]$ ($\lambda\lambda$ 6548.03, 6583.41 Å), $[\text{S II}]$ ($\lambda\lambda$ 6716.47, 6730.85 Å), and $\text{H}\alpha$ are reported in: Tables 4–7 for NGC 2179; Tables 10–14 for NGC 2775; Tables 17–21 for NGC 3281; Tables 24–26 for

IC 724; Tables 29–33 for NGC 4698; and Tables 36–40 for NGC 4845. Each table reports the galactocentric distance r in arcsec (Col. 1), the observed heliocentric velocity v and its error δv in km s^{-1} (Col. 2), the velocity dispersion σ in km s^{-1} (Col. 3), the number n of spectrum rows binned along the spatial direction (Col. 4), and the signal-to-noise ratio S/N of the emission line (Col. 5). The $\text{H}\alpha$, $[\text{N II}]$ and $[\text{S II}]$ kinematics of the sample objects are plotted in Figs. 2–4.

The final ionized-gas kinematics is obtained by averaging, at each radius, the gas velocities and velocity dispersions derived independently from the different emission lines. The gas velocity (v_g) and velocity error (δv_g) are respectively the $1/\sigma_v^2$ -weighted mean velocity and its uncertainty. The gas velocity dispersion (σ_g) and velocity-dispersion error ($\delta\sigma_g$) are the mean velocity dispersion and its uncertainty. (No error is given when only one velocity dispersion measurement is available.)

The kinematics of the ionized gas is reported in: Table 8 for NGC 2179; Table 15 for NGC 2775; Table 22 for NGC 3281; Table 27 for IC 724; Table 34 for NGC 4698; and Table 41 for NGC 4845. Each table reports the galactocentric distance r in arcsec (Col. 1), the mean heliocentric velocity v_g and its error δv_g in km s^{-1} (Col. 2), the mean velocity dispersion σ_g and its error $\delta\sigma_g$ in km s^{-1} (Col. 3). The ionized-gas velocity and velocity-dispersion profiles are plotted in Fig. 5 for all our galaxies.

2.1.3. Measuring the stellar kinematics

The stellar velocities (v_*) and velocity dispersions (σ_*) of the sample galaxies were measured from the absorption lines in the wavelength range between about 5200 Å and 6200 Å. We used an interactive version of the Fourier Quotient Method (Sargent et al. 1977) as applied by Bertola et al. (1984). The KOIII star HR 5100 was taken as template: it has a radial velocity of -0.9 km s^{-1} (Wilson 1953) and a rotational velocity of 10 km s^{-1} (Bernacca & Perinotto 1970).

The spectra of the galaxies and the template star were rebinned to a logarithmic wavelength scale, continuum subtracted, and masked at their edges by means of a cosine bell function of 20% length. At each radius the galaxy spectrum was assumed to be the convolution of the template spectrum with a Gaussian broadening function characterized by the parameters γ , v_* and σ_* . They respectively represent the line strength of the galaxy spectrum relative to the template’s, and the line-of-sight stellar velocity and velocity dispersion. The parameters of the broadening function, and consequently the stellar kinematics, were obtained by a least-squares fitting in the Fourier space of the broadened template spectrum to the galaxy spectrum in the wavenumber range $[k_{min}, k_{max}] = [5, 440]$. In this way we rejected the low-frequency trends (corresponding to $k < 5$) due to the residuals of continuum subtraction and the high-frequency noise (corresponding to $k > 440$) due to the instrumental resolution. (The wavenumber range is important in particular in the Fourier fitting of lines with non-Gaussian profiles, see van der Marel & Franx 1993 and Cinzano & van der Marel 1994). In deriving the above kinematical properties, the

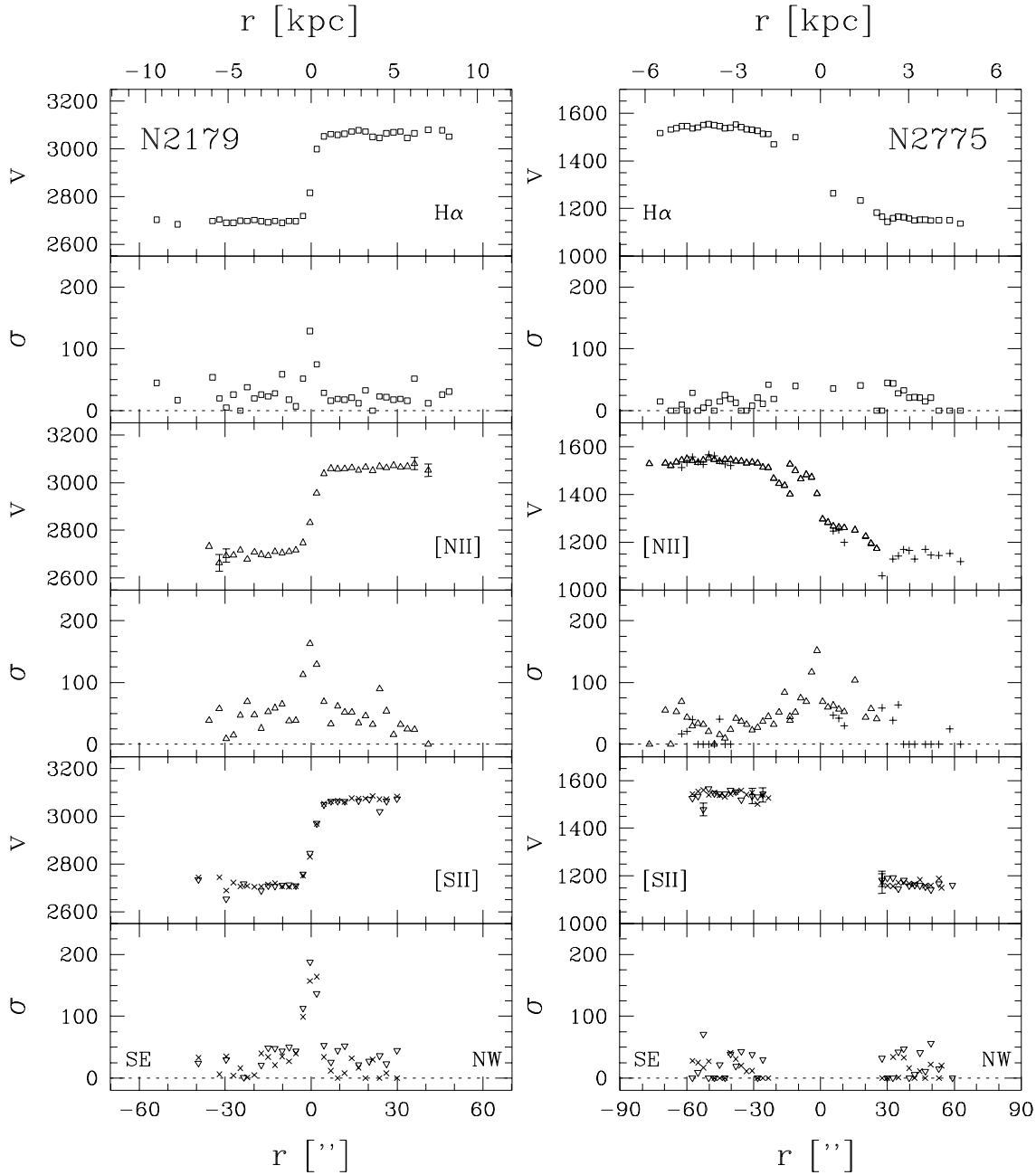


Fig. 2. NGC 2179 and NGC 2775 observed major-axis velocity curves and velocity dispersion profiles of ionized gas. The kinematics measured from the $H\alpha$ line is represented by *open squares* (\square). The *crosses* (+) and the *open triangles* (\triangle) refer to the data obtained from the [N II] ($\lambda\lambda$ 6548.03, 6583.41 Å). The *times* (\times) and the *reversed triangles* (∇) represent kinematics deduced from the [S II] ($\lambda\lambda$ 6716.47, 6730.85 Å) lines. For the velocities only the errors greater than symbols are plotted

regions $5569.0 < \lambda < 5585.0$ Å and $5884.0 < \lambda < 5900.0$ Å were masked because of contamination from bad subtraction of the night-sky emission lines of [O I] (λ 5577.34 Å) and Na I (λ 5889.95 Å).

The measured stellar kinematics is reported in: Table 9 for NGC 2179; Table 16 for NGC 2775; Table 23 for NGC 3281; Table 28 for IC 724; Table 35 for NGC 4698; and Table 42 for NGC 4845. Each table reports the galactocentric distance r in arcsec (Col. 1), the heliocentric velocity v_* and its error δv_* in

km s^{-1} (Col. 2), the velocity dispersion σ_* and its error $\delta\sigma_*$ in km s^{-1} (Col. 3). The stellar velocity and velocity-dispersion profiles are plotted in Fig. 5.

2.2. The photometric observations

The observation in the Cousin R -band of NGC 2179 was performed on March 11, 1997 at the 1.83-m Vatican Advanced Technology Telescope (VATT) at Mt. Graham International O-

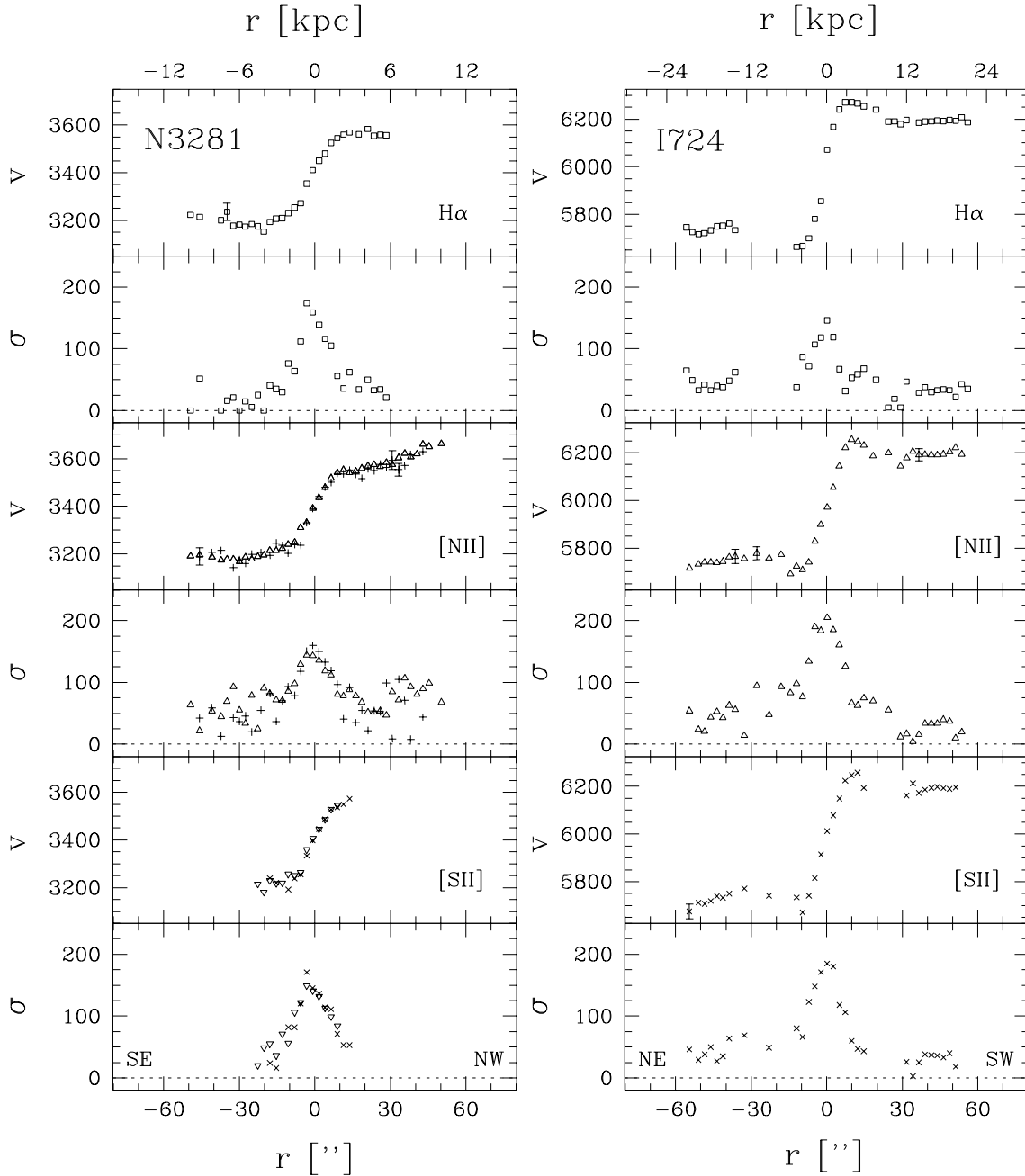


Fig. 3. Same as in Fig. 2, but for NGC 3281 and IC 724

bservatory. A back-illuminated 2048×2048 Loral CCD with $15 \times 15 \mu\text{m}^2$ pixels was used as detector at the aplanatic Gregorian focus, $f/9$. It yielded a field of view of $6'.4 \times 6'.4$ with an image scale of $0''.4 \text{ pixel}^{-1}$ after a 2×2 pixel binning. The gain and the readout noise were $1.4 \text{ e}^- \text{ ADU}^{-1}$ and 6.5 e^- respectively. We obtained 3 images of 120 s with the R 3.48-inch square filter.

The data reduction was carried out using standard IRAF³ routines. The images were bias subtracted and then flat-field

corrected. They were shifted and aligned to an accuracy of a few hundredths of a pixel using field stars as reference. After checking that the point spread functions (PSFs) in the images were comparable, they were averaged to obtain a single R image. The cosmic rays were identified and removed during the averaging routine. A Gaussian fit to the intensity profile of field stars in the resulting image allowed us to estimate a seeing PSF FWHM of $1''.8$.

³ IRAF is distributed by the National Optical Astronomy Observatories which are operated by the Association of Universities for Research

in Astronomy (AURA) under cooperative agreement with the National Science Foundation.

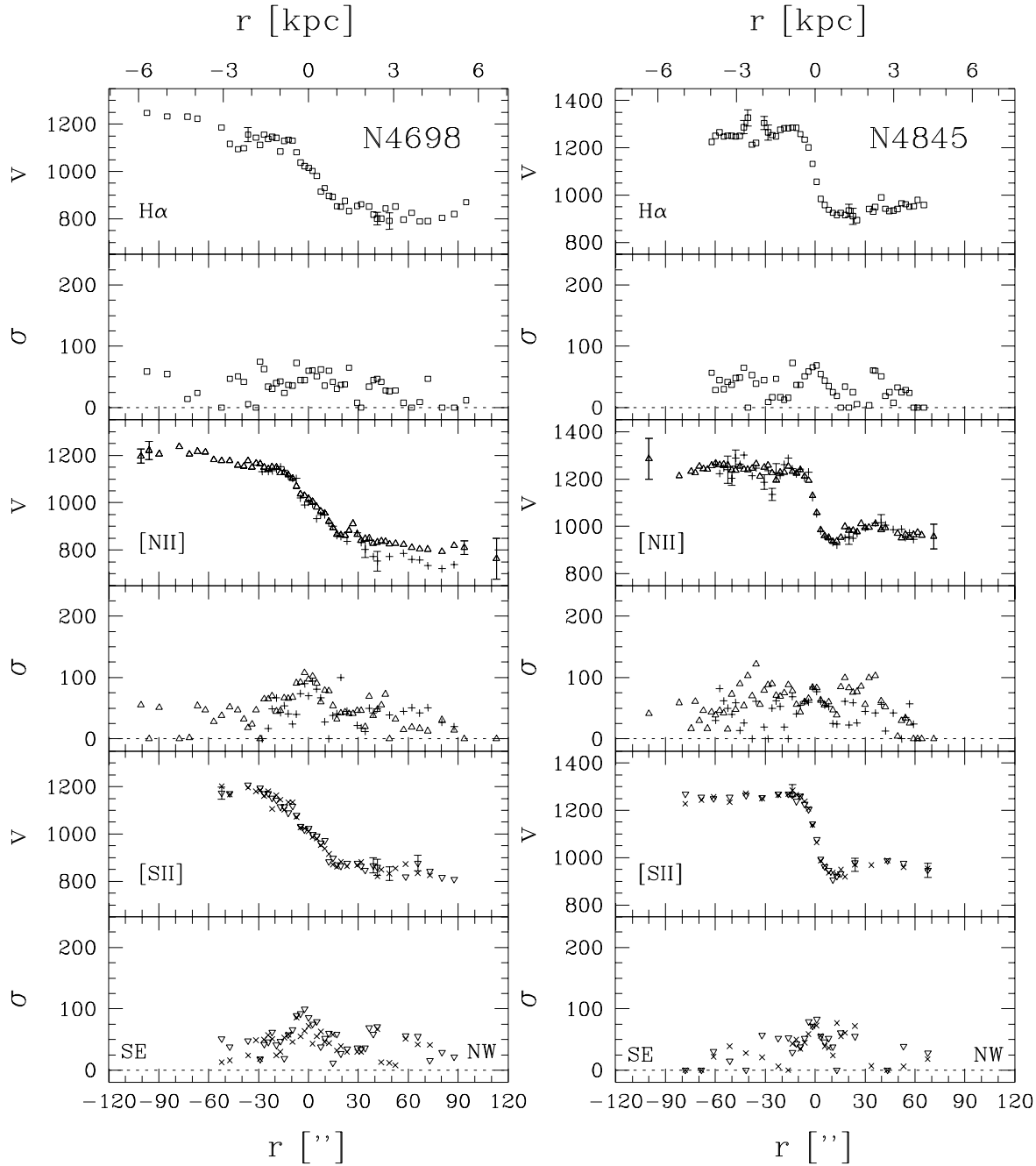


Fig. 4. Same as in Fig. 2, but for NGC 4698 and NGC 4845

The sky subtraction and the elliptical fitting to the galaxy isophotes were performed by means of the Astronomical Images Analysis Package (AIAP; Fasano 1990). The sky level was determined by a polynomial fit to surface brightness in frame regions not contaminated by galaxy light; then it was subtracted out from the total signal. The isophote fitting was performed masking the frame's bad columns and the bright field stars. We then obtained surface brightness, ellipticity, major-axis position angle, and the $\cos 4\theta$ Fourier coefficient of the isophote's deviations from elliptical as a function of radius along the major axis. No photometric standards were observed. Thus the ab-

solute calibration was made using the photometric quantities edited by Lauberts & Valentijn (1989) in the same band. We set the surface brightness of an isophote with semi-major axis of $a = 20''.6$ to the value $\mu = 21.23 R\text{-mag arcsec}^{-2}$.

3. The stellar and ionized gas kinematics

The resulting kinematics of all our galaxies are shown in Fig. 5. The plotted velocities are as observed (no inclination correction is applied). In the following we briefly discuss each individual object. At each radius, V_* ($\equiv |v_* - V_\odot|$) and V_g ($\equiv |v_g - V_\odot|$)

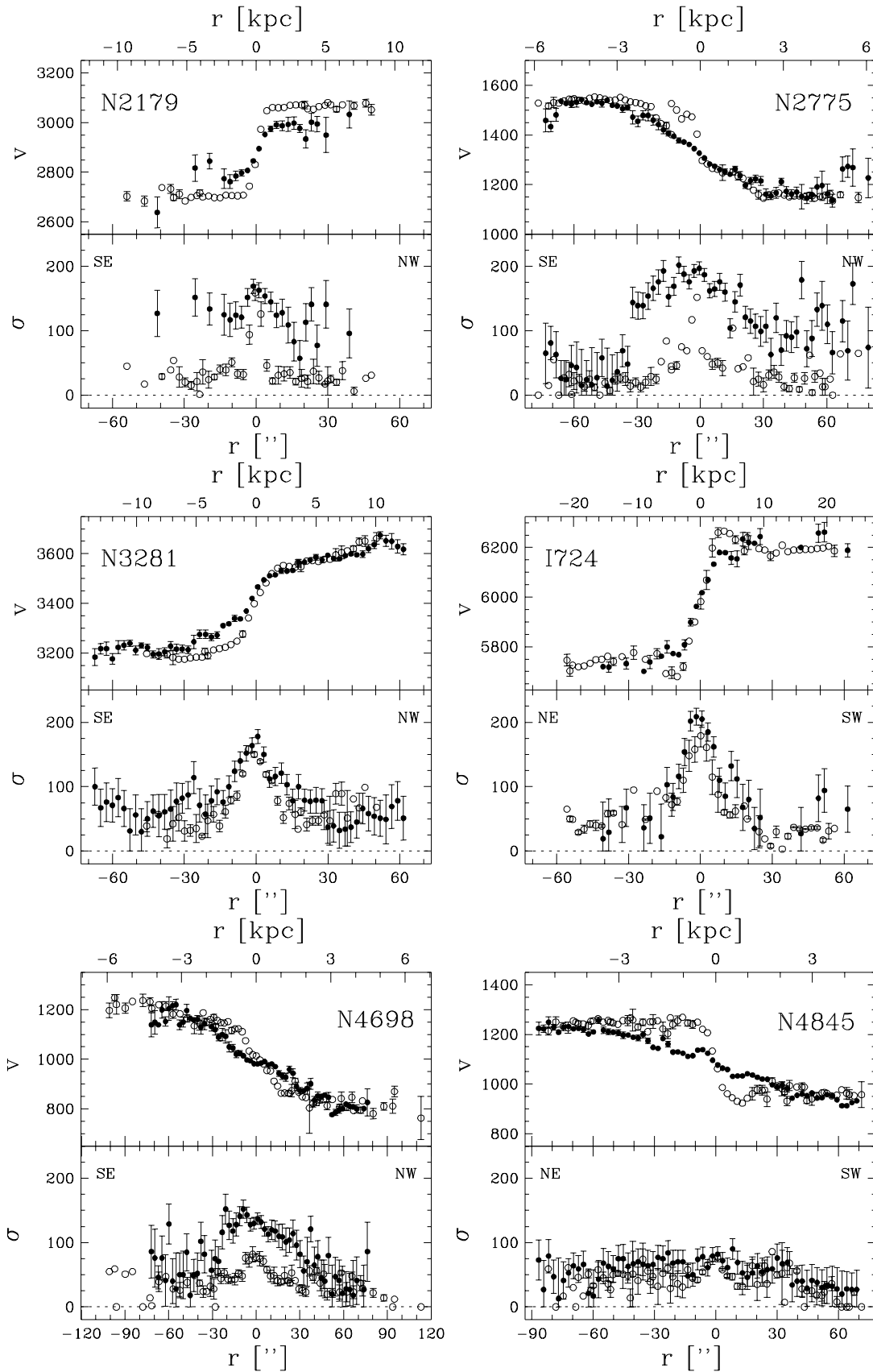


Fig. 5. Major-axis observed velocity curves and velocity dispersion profiles of the stellar (*filled circles*) and the gaseous (*open circles*) components for the sample galaxies. For the velocities the errorbars smaller than symbols are not plotted

are the observed rotation velocities of the stars and the ionized gas, respectively.

NGC 2179. The gas and stellar kinematics respectively extend to $50''$ (8.6 kpc) and $40''$ (6.9 kpc) on either side of the nucleus. Outwards of $40''$, the stellar and the gas radial velocities are comparable.

Stars. In the inner $10''$ (1.7 kpc), V_* increases to $\sim 100 \text{ km s}^{-1}$. At the center $\sigma_* \sim 170 \text{ km s}^{-1}$; away from the nucleus it remains high ($\sigma_* \geq 100 \text{ km s}^{-1}$), and possibly even rises.

Gas. V_g has a steeper gradient than V_* , reaching a value of $V_g = 190 \text{ km s}^{-1}$ at $|r| \sim 6''$ (1.0 kpc). σ_g is strongly peaked ($\sim 150 \text{ km s}^{-1}$) at the center; at $|r| > 6''$ it drops rapidly to $\sigma_g \simeq 30 \text{ km s}^{-1}$.

A circumnuclear Keplerian disk of ionized gas has been recently discovered in the center of NGC 2179 by Bertola et al. (1998a) by means of optical ground-based observations. By modeling the motion of the gaseous disk they inferred the presence of a central mass concentration of $10^9 M_\odot$.

NGC 2775. The gas and stellar kinematics is measured out to $80''$ (6.1 kpc) from the center.

Stars. V_* increases almost linearly with radius, up to about 130 km s^{-1} at $|r| \sim 22''$ (1.7 kpc); for $22'' \leq |r| \leq 30''$ it remains approximately constant; further out it increases to 185 km s^{-1} and then flattens out. At $-30'' \leq r \leq +20''$, $\sigma_* > 150 \text{ km s}^{-1}$; farther out it declines to $\sim 40 \text{ km s}^{-1}$ and $\sim 100 \text{ km s}^{-1}$ in the SE and NW side, respectively.

Gas. The gas behaves differently in the two regions $|r| \leq 20''$ (1.5 kpc) and $|r| > 20''$. The [N II] $\lambda 6583.41$ line (the only emission line detected in both regions, see Fig. 2) shows the presence of two kinematically distinct gas components, named component (i) and (ii). Component (i) rotates with the same velocity as the stars but with a lower velocity dispersion; component (ii) rotates faster than the stars for $0 > r \gtrsim -15''$ (1.1 kpc). Both components show up simultaneously in the spectrum only at $|r| \simeq 14''$, where a double peak in the emission line is clearly detected. σ_g peaks (160 km s^{-1}) at the center and rapidly drops to $\sim 30 \text{ km s}^{-1}$ off center.

NGC 3281. The stellar kinematics extends to $90''$ (18 kpc) and $60''$ (12 kpc) in the SE and the NW side, respectively. The gas kinematics can only be measured within $50''$ (10 kpc) on each side of the nucleus.

Stars. The stars exhibit a rather shallow rotation gradient: at $r = 10''$ (2 kpc), $V_* \sim 100 \text{ km s}^{-1}$. At the center $\sigma_* \sim 180 \text{ km s}^{-1}$; off center it decreases to, respectively, $\sim 70 \text{ km s}^{-1}$ in the SE side and $\sim 50 \text{ km s}^{-1}$ in the NW side.

Gas. V_g has a steep gradient, reaching 150 km s^{-1} at $10''$ and then 200 km s^{-1} at $20''$ (4 kpc). At the center $\sigma_g \sim 160 \text{ km s}^{-1}$, while at $|r| > 20''$ it falls to $\sim 50 \text{ km s}^{-1}$; $\sigma_g \sim \sigma_*$ for $|r| < 10''$.

IC 724. The stellar kinematics is observed out to $60''$ (22.7 kpc) and $40''$ (15.1 kpc) in the SW and NE sides, respectively. The ionized-gas kinematics extends to $60''$ on each side of the nucleus. For $|r| > 20''$ (7.6 kpc), the gas and stellar kinematics are similar. For $|r| < 20''$, σ_g is centrally peaked at $\sim 180 \text{ km s}^{-1}$, remaining lower than σ_* .

Stars. V_* increases linearly up to $\sim 200 \text{ km s}^{-1}$ in the inner $8''$ (3.0 kpc), followed by a drop to $\sim 170 \text{ km s}^{-1}$ between $8''$ and $15''$ on both sides of the nucleus; further out it rises to $\sim 240 \text{ km s}^{-1}$ at $20''$, and then remains constant. At the center $\sigma_* \sim 210 \text{ km s}^{-1}$, then off the nucleus it decreases to $\sim 50 \text{ km s}^{-1}$.

Gas. V_g has a steeper gradient than V_* , peaking at 300 km s^{-1} at about $8''$; then it decreases, becoming $V_g \sim V_*$ at $20''$. The H α shows steeper central RC gradient and lower velocity dispersion than [N II] and [S II] (see Fig. 3). This feature is probably due to the lower V_* : the H α absorption does not have the same central wavelength as the emission, and hence it shifts the resulting peak toward higher rotation velocities.

NGC 4698. The stellar and ionized-gas kinematics are measured out to $75''$ (4.4 kpc) and $100''$ (5.9 kpc) on each side of the nucleus, respectively.

Stars. In the innermost $10''$ (0.6 kpc) the stars have zero rotation; at outer radii, V_* is less steep than V_g ; only for $|r| > 40''$ (2.3 kpc) are $V_* \sim V_g$ and $\sigma_* \sim \sigma_g$. The profile of σ_* is radially asymmetric: in the SE side it shows a maximum of $\sim 150 \text{ km s}^{-1}$ at $9''$ (0.5 kpc), then it decreases outwards to ~ 50 and 30 km s^{-1} at $30''$ (1.8 kpc) in the SE and NW sides, respectively. The measured zero rotation plateau is explained by Bertola et al. (1998b) as due to the presence of an orthogonal-rotating bulge.

Gas. V_g increases to $\sim 130 \text{ km s}^{-1}$ in the inner $18''$ (1.1 kpc); then it increases more gradually reaching $\sim 200 \text{ km s}^{-1}$ at $60''$ (3.5 kpc), and stays approximately constant farther out. In the inner $\pm 7''$ (± 0.4 kpc, roughly coinciding with the absorption lines region) σ_g has a 75 km s^{-1} plateau, while at larger radii it drops to $\sigma_g \leq 50 \text{ km s}^{-1}$.

NGC 4845. The stellar and ionized-gas kinematics are measured out to $70''$ (4.4 kpc) in the SW side, and out to $90''$ (5.7 kpc) in the NE side.

Stars. V_* has a shallower gradient than V_g : it reaches 60 km s^{-1} at $8''$ (0.5 kpc), and further out it increases slowly, reaching the V_g at $\sim 60''$ (3.8 kpc). The velocity dispersion is constant, $\sigma_* \sim 60 \text{ km s}^{-1}$ (in the SW side it drops to 30 km s^{-1} for $r > 40''$).

Gas. V_g reaches $\sim 180 \text{ km s}^{-1}$ at $14''$ (0.9 kpc), to decrease and remain constant at 150 km s^{-1} farther out. For $|r| < 10''$ (0.6 kpc) $\sigma_g \simeq 80 \text{ km s}^{-1}$, then it rapidly falls to < 30 and $\sim 40 \text{ km s}^{-1}$ in the SW and NE sides, respectively; farther out the behavior of σ_g is more uncertain, due to a considerable scatter of the measurements from different lines: along the NW side

$\sigma_g \sim 40 \text{ km s}^{-1}$, while along the SE side σ_g slowly decreases to $\sim 30 \text{ km s}^{-1}$.

The triaxiality of the bulge of NGC 4845 has been detected by Bertola, Rubin & Zeilinger (1989) and discussed by Gerhard, Vietri & Kent (1989).

The RCs and velocity-dispersion profiles of both the ionized gas and the stars in our Sa galaxies show a rich diversity of kinematical properties.

V_* has shallower gradient than V_g at the center, while $V_* = V_g$ at the last measured radius, in all our sample galaxies. For NGC 2179, NGC 2775, NGC 3593, NGC 4698 and NGC 4845, the gas RCs remain flat after a monotonic rise to a maximum [whose observed values range between $\sim 120 \text{ km s}^{-1}$ (as for NGC 3593) and $\sim 190 \text{ km s}^{-1}$ (as for NGC 2179, NGC 2775)], or rise monotonically to the farthest observed radius (as for NGC 3281 and IC 724: in the latter after an initial peak at $\sim 290 \text{ km s}^{-1}$). Stellar counterrotation and orthogonal rotation have been found in NGC 3593 (Bertola et al. 1996) and NGC 4698 (Bertola et al. 1998b) respectively.

The observed σ_* exceeds 100 km s^{-1} for several kpc in the innermost regions, peaking at values ranging between 130 km s^{-1} (as in NGC 4698) and 210 km s^{-1} (as in IC 724); the only exception is NGC 4845 with $\sigma_* \sim 70 \text{ km s}^{-1}$ at all observed radii. There are sample galaxies whose σ_g is low at all radii, reaching a central maximum of $\sim 80 \text{ km s}^{-1}$ (NGC 4698, NGC 4845) or remaining flattish at $\sim 50 \text{ km s}^{-1}$ (NGC 3593); and others where σ_g increases to $> 100 \text{ km s}^{-1}$ either at the very center (as in NGC 2179, NGC 2775) or over an extended radial range around the center (as in NGC 3281, IC 724).

4. Mass models

Previous authors (Fillmore, Boroson & Dressler 1986; Kent 1988; Kormendy & Westpfahl 1989) noticed that in the bulge of early-type spirals V_g falls below the predicted circular velocity. Such ‘slowly rising’ gas RCs are explained by Bertola et al. (1995) with the argument that random (non-circular) motions are crucial for the dynamical support of the ionized gas: in some galaxies of their S0 sample they measured $\sigma_g \sim \sigma_* \gtrsim 150 \text{ km s}^{-1}$ over an extended range of radii. We do observe the same phenomenon in some of our early-type spirals (see Fig. 5): this fact prevents us to adopt, for early-type disk galaxies, the inner portion of $V_g(r)$ as the circular velocity on which to perform the mass decomposition. When the high values for the velocity dispersion of the gas are measured only in the very central parts (as in NGC 2179) we can not exclude that this is an effect of rotational broadening due to the seeing smearing of the steep velocity gradient.

At larger radii where $\sigma_g \lesssim 50 \text{ km s}^{-1}$, the ionized gas can be considered a tracer of the actual circular velocity. But the limited extension, $(0.5-1) R_{25}$ (see Table 1), of our $V_g(r)$ makes the derivation of the halo parameters of early-type spirals more uncertain than for later types. In fact, on one hand we lack data at very large radii where only disk and halo affect the circular velocity, on the other hand at small radii (where we can not consider the gas in circular motion) not two (like for

Sc-Sd galaxies), but three mass components will have locally similar behaviors (solid-body like). So, in absence of extended and complete RCs, an Sa mass solution would be degenerate.

We therefore have to model the stellar kinematics to determine the galaxy’s total gravitational potential. Then we need to check the derived mass decomposition by comparing the circular velocity, inferred from the model, with V_g at large galactocentric radii. This is necessary to minimize uncertainties on the mass structure obtained from the stellar kinematics. In fact, the uncertain orbital structure of the spheroidal component, consistent with the observed kinematics leads to a degeneracy between velocity anisotropy and mass distribution, which can be solved only through the knowledge of the line-of-sight velocity distribution profiles (Gerhard 1993).

Two galaxies of the observed sample, namely NGC 2179 and NGC 2775, are particularly suited to be studied with the three-component mass models, based on stellar photometry and kinematics, at our disposal. They were chosen for their nearly axisymmetric stellar pattern and to not contain kinematically decoupled (as found NGC 3593 and NGC 4698) or triaxial (as found in NGC 4845) stellar components.

4.1. The modeling technique

We apply the Jeans modeling technique introduced by Binney, Davies & Illingworth (1990), developed by van der Marel, Binney & Davies (1990) and van der Marel (1991), and extended to two-component galaxies by Cinzano & van der Marel (1994) and to galaxies with a DM halo by Cinzano (1995). (For a detailed description of the model and its assumptions, see the above references.)

The galaxy is assumed to be axisymmetric. Its mass structure results from the contributions of: (i) a spheroidal component; (ii) an infinitesimally thin exponential disk; and (iii) a spherical pseudo-isothermal dark halo with density distribution $\rho(r) = \rho_0 / [1 + (r/r_h)^2]$. The mass contribution of the ionized gas is assumed to be negligible at all radii. The spheroidal and disk components are supposed to have constant M/L ratios. The total potential is the sum of the (numerically derived) potential of the spheroid plus the (analytical) potentials of the disk and the halo.

The stellar distribution function f is assumed to depend only on two integral of motion [i.e., $f = f(E, L_z)$]. In these hypotheses the Jeans equations for hydrostatic equilibrium form a closed set that, once solved in the total potential, yields the dynamical quantities to be compared with the observed kinematics, once projected onto the sky plane.

To obtain the potentials of the bulge and the disk, we proceed through several steps. (a) First, the bulge surface brightness is derived from the total one by subtracting the disk. Then, it is deprojected by means of Lucy’s algorithm to yield the 3-D luminosity density which, via the M/L ratio, gives the 3-D mass density of the bulge. Finally, solving Poisson’s equation through multipole expansion, we derive the bulge potential (Binney et al. 1990). (b) The exponential disk parameters (scale length r_d , central surface brightness μ_0 , and inclination i) are chosen ac-

cording to the best-fit photometric decomposition. If $\overline{r_d}$, $\overline{\mu_0}$ and \overline{i} are the disk parameters resulting from the photometric decomposition, the best-fit model to the observed stellar kinematics was obtained considering exponential disks with $|r_d - 2''| \leq \overline{r_d}$, $|\mu_0 - 0.3| \text{ mag arcsec}^{-2} \leq \overline{\mu_0}$, and $|i - 5^\circ| \leq \overline{i}$. These parameters determine the surface brightness of the disk. Through the disk M/L ratio we obtain the surface mass density of the disk, and then its potential (Binney & Tremaine 1987).

We first solved the Jeans equations only for both the bulge and disk components in their total potential, to give in every point of the galaxy the velocity dispersions onto the meridional plane $\sigma_R^2 = \sigma_z^2$ and the mean azimuthal squared velocities $\overline{v_\phi^2}$.

To disentangle the respective contributions of the azimuthal velocity dispersion σ_ϕ^2 and the mean stellar motion $\overline{v_\phi^2}$ to $\overline{v_\phi^2}$, for the bulge we made the same hypotheses of Binney et al. (1990) while for the disk we followed Cinzano & van der Marel (1994) respectively. Part of the second azimuthal velocity moment $\overline{v_\phi^2}$ in the bulge is assigned to the streaming velocity $\overline{v_\phi}$ as in Satoh (1980). The azimuthal velocity dispersion σ_ϕ^2 in the disk is assumed to be related to σ_R^2 (which is assumed in turn to have an exponential fall-off with central value $\sigma_{R,0}^2$ and scale-length r_σ) according to the epicyclic theory (cfr. Binney & Tremaine 1987).

In the framework of Cinzano & van der Marel (1994), we have to take into account the effects of seeing, of finite slit-width and pixel-size in data acquisition, and of Fourier filtering in data reduction (notably the wavenumber range, as discussed in Sect. 2.1.), in order to compare the sky-projected model predictions with the observed stellar kinematics.

We interpret the discrepancy between the model's circular velocity and the observed gas rotation in the outer regions as due to the presence of a DM halo. In this case, the Jeans equations have to be solved again, taking the halo into account, too. By introducing the DM halo, the number of free parameters of the model increases to ten. They are: k , the local rotation anisotropy parameter of the bulge; the M/L ratios of the bulge and the disk; the disk central surface brightness, scale length and inclination; the central value and scale length of the disk's second radial velocity moment; and the halo's central mass density and core radius. To reduce the number of free parameters, in the following we consider only three-component models having same best-fit parameters as no-halo models except for the bulge and disk M/L ratios. We choose the fit parameters in order to simultaneously reproduce the stellar kinematics at all radii as well as V_g at large radii.

The modeling technique described above derives the 3-D distribution of the luminous mass from the 3-D luminosity distribution inferred from the observed surface photometry. For this reason, in the central regions we take into account the seeing effects on the measured photometrical quantities (surface brightness, ellipticity and $\cos 4\theta$ deviation profiles).

We derive for NGC 2179 and NGC 2775 the seeing cutoffs r_μ and r_ϵ , defined by Peletier et al. (1990) as the radii beyond which the seeing-induced error on the profile is lower than, respectively, $0.05 \text{ mag arcsec}^{-2}$ in surface brightness and 0.02

in ellipticity. They have expressed r_μ and r_ϵ for a de Vaucouleurs profile as a function of the seeing FWHM, the effective radius r_e and the ellipticity ϵ . For the bulge, we obtained r_e and ϵ , and the corresponding seeing cutoffs r_μ and r_ϵ , following an iterative procedure. We started by performing a standard bulge-disk decomposition with a parametric fit (e.g. Kent 1985): we decomposed the observed surface-brightness profile on both the major and the minor axis as the sum of a de Vaucouleurs bulge of surface-brightness profile

$$\mu_b = \mu_e + 8.3268 \left[\left(\frac{r}{r_e} \right)^{1/4} - 1 \right], \quad (2)$$

plus an exponential disk of surface-brightness profile

$$\mu_d = \mu_0 + 1.0857 \left(\frac{r}{r_d} \right). \quad (3)$$

We assumed the minor-axis profiles of each component to be the same as the major-axis profiles, with values scaled by a factor $1 - \epsilon = b/a$. A least-squares fit of the model to the photometric data provided r_e , μ_e and ϵ of the bulge, μ_0 , r_d of the disk, and the galaxy inclination i . The values of r_e and ϵ were used as a starting input to derive r_μ and r_ϵ . Following van der Marel (1991), the ellipticity ϵ and the $\cos 4\theta$ Fourier coefficients were kept constant within r_ϵ to their value at r_ϵ , and the surface-brightness profile was truncated at its value at r_μ . A new parametric bulge-disk decomposition was then performed on the truncated photometric data. The resulting new values of the effective radius and ellipticity of the bulge were in turn used to obtain a further estimate of r_μ and r_ϵ . The surface photometry was again modified according to these new values, and then another parametric fitting was done. The process was repeated up to convergence.

A least-squares fit to $\mu(r)$ in the bulge-dominated region beyond r_μ was performed using the 2-D brightness distribution resulting from the 3-D luminosity density given for a spherical body by:

(i) a modified Hubble law (Rood et al. 1972):

$$j_{hu}(r) = j_0 \left[1 + \left(\frac{r}{a_{hu}} \right)^2 \right]^{-\frac{3}{2}} \quad (4)$$

where j_0 and a_{hu} are respectively the central luminosity density and the core radius;

(ii) a Jaffe law (Jaffe 1983):

$$j_{ja}(r) = \frac{L_{tot}}{4\pi a_{ja}^3} \left(\frac{a_{ja}}{r} \right)^2 \frac{1}{(1 + r/a_{ja})^2} \quad (5)$$

where L_{tot} and a_{ja} are the total luminosity and the half-light radius;

(iii) a Hernquist law (Hernquist 1990):

$$j_{he}(r) = \frac{L_{tot}}{2\pi} \frac{a_{he}}{r} \frac{1}{(r + a_{he})^3} \quad (6)$$

where L_{tot} and a_{he} are the total luminosity and a scale radius.

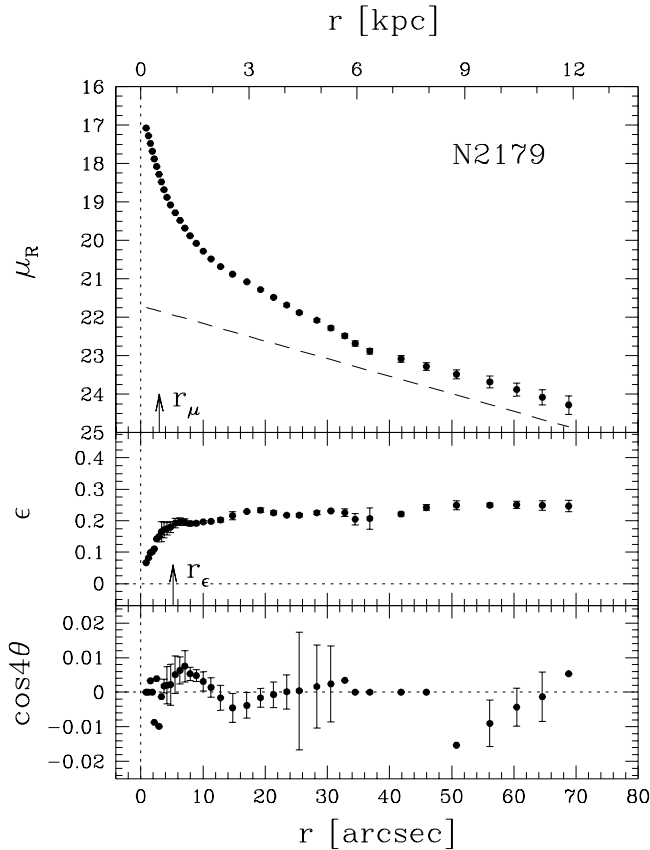


Fig. 6. The NGC 2179 R -band surface brightness, ellipticity and $\cos 4\theta$ coefficient profiles as a function of radius along the major axis. The arrows in the surface brightness and in the ellipticity panels indicate the position of the seeing cutoff radii r_μ and r_ϵ . The *dashed curve* in the upper panel is the surface brightness exponential profile of the disk component of the best fit model to the stellar kinematics

The best fit was achieved for NGC 2179 with a Hernquist profile and for NGC 2775 with a modified Hubble profile. We used them to extrapolate the $\mu(r)$ profiles of the two galaxies to $r < r_\mu$. After subtracting the disk contribution from the total surface brightness, the 3-D luminosity density of the bulge was obtained starting Lucy’s iterations from a flattened Hernquist model for NGC 2179 and from a flattened modified Hubble model for NGC 2775. The radial profiles of these flattened models are derived respectively from Eqs. 6 and 4 by replacing r with $(q^2 R^2 + z^2)^{1/2}$ where q is the flattening and R, z cylindrical coordinates.

4.2. The modeling results

In this section we present the mass models of NGC 2179 and NGC 2775.

4.2.1. NGC 2179

In Fig. 6 we show the R -band surface brightness (μ_R), ellipticity (ϵ) and $\cos 4\theta$ Fourier coefficient of the isophote deviations from elliptical, as a function of radius along the major axis.

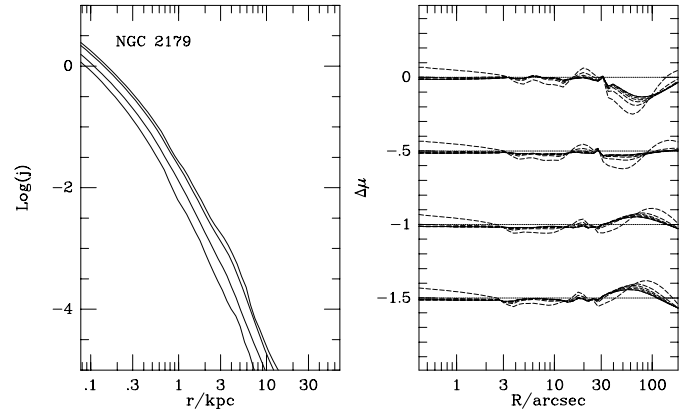


Fig. 7. The deprojection of the surface brightness of the spheroidal component of NGC 2179. The *right panel* shows the difference $\mu_{\text{model}} - \mu_{\text{obs}}$ after each Lucy iteration (*dashed lines*) starting from an initial Hernquist fit to the actual NGC 2179 bulge brightness. The residuals are shown for four axes (major through minor axis: top through bottom). For each set of curves: the *solid line* corresponds to the projected adopted model for 3-D luminosity density; and the *dotted line* corresponds to a perfect deprojection. At each iteration if the model is brighter than the galaxy, the corresponding *dashed* or *continuous* curve is below the *dotted line*. In the *left panel* the final 3-D luminosity density profile of the spheroidal components of NGC 2179 is given in units of $10^{10} L_\odot \text{ kpc}^{-3}$ for the same four axes (minor through major axis: innermost through outermost curve)

The seeing cutoffs are $r_\mu = 3''.0$ and $r_\epsilon = 5''.2$. The corresponding best-fit parameters obtained from the photometric decomposition are: $\mu_e = 21.0 R\text{-mag arcsec}^{-2}$, $r_e = 12''.4$, $\epsilon_b = 0.58$ for the de Vaucouleurs bulge; $\mu_0 = 21.8 R\text{-mag arcsec}^{-2}$, $r_d = 23''.5$, $\epsilon_d = 0.29$ for the exponential disk. (Taking into account the photometric bulge-disk decomposition, the exponential disk yielding the best-fit model to the observed stellar kinematics has $\mu_0 = 21.7 R\text{-mag arcsec}^{-2}$, $r_d = 23''.7 = 4.1 \text{ kpc}$, and $i = 45^\circ$; see *dashed curve* in Fig. 6). We then subtract the disk contribution from the total surface brightness. The residual surface brightness is the contribution of the spheroidal component.

The difference between the surface brightness of the spheroid and that obtained projecting the 3-D luminosity distribution of each of the four Lucy iterations (including the initial flattened Hernquist model) is shown in Fig. 7 (right panel) along NGC 2179’s major, minor and two intermediate axes. (The r.m.s. residual of the last Lucy iteration corresponds to $0.06509 \text{ mag arcsec}^{-2}$). The 3-D luminosity density of the final bulge model along the same four axes is also presented in Fig. 7 (left panel).

We fold v_g and v_* around their respective centers of symmetry. In order to determine the latter, we fit a suitable odd function to both RCs independently: this yields the position of the kinematical center of the curve, r_0 , and the heliocentric velocity of the galaxy, V_\odot . We find $V_\odot = 2885 \pm 10 \text{ km s}^{-1}$ for both gas and stars, and $r_{0,g} = +0''.5 \pm 0''.3$ and $r_{0,*} = +0''.6 \pm 0''.3$. We then fold σ_g and σ_* around the kinematical center of the respective component.

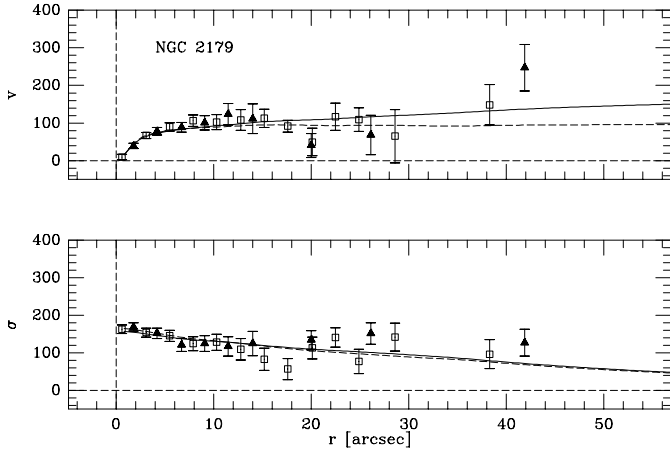


Fig. 8. Predicted and observed stellar kinematics of NGC 2179. The *filled triangles* and the *open squares* represent data derived for the approaching SE side and for the receding NW side respectively. The *continuous* and the *dashed lines* are the model stellar velocities (*upper panel*) and velocity dispersions (*lower panel*) obtained with and without the dark halo component respectively

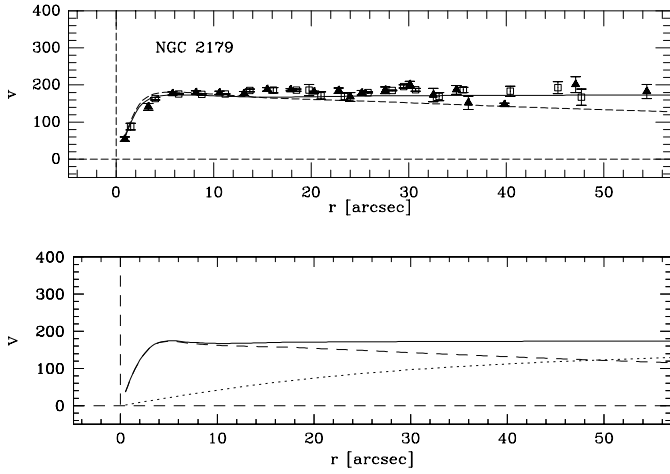


Fig. 9. In the *upper panel* the predicted circular velocity and the observed gas rotation velocity of NGC 2179 are shown. The *filled triangles* and the *open squares* represent data derived for the approaching side and for the receding side respectively. The *continuous* and the *dashed lines* are the total circular velocities derived from the stellar kinematics with and without the dark halo component respectively. In the *lower panel* the maximum contribution of the luminous matter (*dashed line*) to the total circular velocity (*continuous line*) is plotted if a dark matter halo (*dotted line*) is considered

The best-fit model to the observed major-axis stellar kinematics is shown in Fig. 8. Its parameters are as follows. The bulge is an oblate isotropic rotator ($k = 1$) with $(M/L_R)_b = 6.1 (M/L_R)_\odot$. The exponential disk has $\sigma_*(r) = 168 e^{-r/r_\sigma} \text{ km s}^{-1}$ with scale-length $r_\sigma = 23''.2 = 4.0 \text{ kpc}$, and $(M/L_R)_d = 6.1 (M/L_R)_\odot$. The derived bulge and disk masses are $M_b = 7.0 \cdot 10^{10} M_\odot$ and $M_d = 2.5 \cdot 10^{10} M_\odot$, adding up to a total (bulge + disk) luminous mass of $M_{LM} = 9.5 \cdot 10^{10} M_\odot$. The DM halo has $\rho_0 = 6.9 \cdot 10^{-2} M_\odot \text{ pc}^{-3}$ and $r_h = 24'' = 4.2 \text{ kpc}$, which correspond to an asymptotic

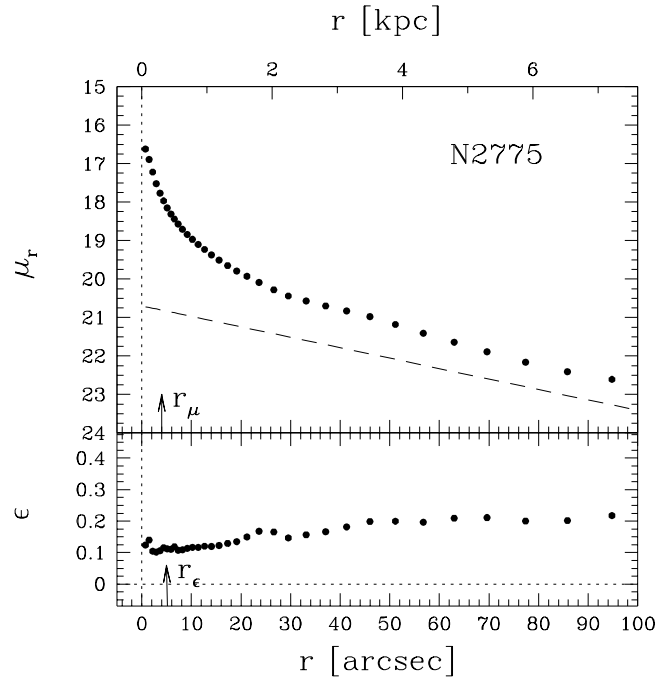


Fig. 10. The NGC 2775 r -band surface brightness and the ellipticity profiles as a function of radius along the major axis (Kent 1988). The *dashed curve* in the *top panel* is the surface brightness exponential profile of the disk component of the best fit model to the stellar kinematics

rotation velocity $V_\infty = 257 \text{ km s}^{-1}$; its mass at the outermost observed radius is $M_{DM} = 6.5 \cdot 10^{10} M_\odot$. The ratio between the mass-to-light ratios of the stellar components in the models with and without the DM halo is 0.9.

The comparison between the observed rotation of the ionized gas and the true circular velocity, inferred from stellar kinematics, is given in the upper panel Fig. 9. It shows that a DM halo is unambiguously required to explain the rotation at large radii ($r \geq 25''$). This result hinges on accuracy of the gas kinematics data beyond $40''$ mostly derived from $H\alpha$ line measurements. In NGC 2179, the gas rotation does provide the circular velocity at all radii. The contribution of the DM halo to NGC 2179 circular velocity as function of radius is plotted in lower panel of Fig. 9.

4.2.2. NGC 2775

In Fig. 10 we show $\mu_r(r)$ and $\epsilon(r)$ along the major axis (Kent 1988). The seeing FWHM for the Kent (1988) data is $2''.3$. We derive the seeing cutoffs $r_\mu = 4''.0$ and $r_\epsilon = 5''.2$. As no $\cos 4\theta$ profile is available, we assume it is zero throughout.

The photometric model is improved by taking into account an outer dust lane surrounding the spiral pattern of the galaxy. (This appears as a thin dust ring at about $80''$ from the center, and is visible on panels 78 and 87 of the CAG, see Sandage & Bedke 1994). As a fitting function for the disk component, we use an exponential profile weighted by an absorption ring. We assume the section of the dust ring to have a Gaussian radial profile,

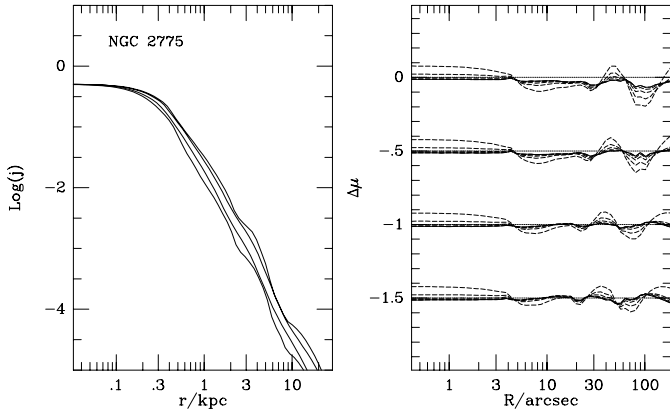


Fig. 11. Same as Fig. 7, but for NGC 2775 and starting from a flattened modified Hubble model for the spheroidal component

defined by central intensity maximum absorption A_r , a center r_r and a scale-length σ_r . This leads to a disk light contribution

$$I_{d,ring}(r) = I_d(r) \left(1 - A_r e^{-\left(\frac{r-r_r}{\sigma_r}\right)^2} \right) \quad (7)$$

The best-fit parameters resulting from the improved photometric decomposition are: $\mu_e = 22.0$ r -mag arcsec $^{-2}$, $r_e = 53''$, $\epsilon_b = 0.10$ for the de Vaucouleurs bulge; $\mu_0 = 20.7$ r -mag arcsec $^{-2}$, $r_d = 40''$, $\epsilon_d = 0.28$ for the exponential disk; and $A_r = 0.25$, $r_r = 85''$ and $\sigma_r = 20''$ for the dust ring. The exponential disk yielding to the best-fit model to the observed stellar kinematics has $\mu_0 = 20.7$ r -mag arcsec $^{-2}$, $r_d = 40'' = 3.0$ kpc, and $i = 44^\circ$ (see Fig. 10).

The surface brightness of the exponential disk in Fig. 10 is subtracted from the total surface brightness. The fit to the spheroidal component's deprojected surface brightness is obtained after four Lucy iterations from an initial flattened modified Hubble model (The r.m.s. residual is 0.03209 mag arcsec $^{-2}$, see Fig. 11). The 3-D luminosity density of the final bulge model along the major, minor and two intermediate axes is also shown in Fig. 11.

We find v_g and v_* to have same center of symmetry at $r_{0,g} = r_{0,*} = +4'' \pm 0''$ and $V_\odot = 1350 \pm 10$ km s $^{-1}$. The velocity dispersion profiles are folded around the kinematical center.

The best-fit model to the observed major-axis stellar kinematics is shown in Fig. 12. Its parameters are as follows. The bulge is an oblate isotropic rotator ($k = 1$) with $(M/L_r)_b = 5.2 (M/L_r)_\odot$. The exponential disk has $\sigma_*(r) = 130 e^{-r/r_\sigma}$ km s $^{-1}$ with scale-length $r_\sigma = 17''$ (1.3 kpc), and $(M/L_r)_d = 7.0 (M/L_r)_\odot$. The derived bulge and disk masses are $M_b = 8.5 \cdot 10^{10} M_\odot$ and $M_d = 6.1 \cdot 10^{10} M_\odot$, so the total (bulge + disk) luminous mass is $M_{LM} = 14.6 \cdot 10^{10} M_\odot$. We kept the ratio between the bulge and disk M/L fixed at the value 1.36 (see Kent 1988). The DM halo has central density $\rho_0 = 5.8 \cdot 10^{-2} M_\odot$ pc $^{-3}$ and core radius $r_h = 60'' = 4.6$ kpc, which correspond to an asymptotic rotation velocity $V_\infty = 258$ km s $^{-1}$; its mass at the outermost observed radius is $M_{DM} = 3.1 \cdot 10^{10} M_\odot$. (The latter should be considered an upper limit because the inner kinematics can be explained with no DM halo). Contrary to NGC 2179 in this case we kept the same

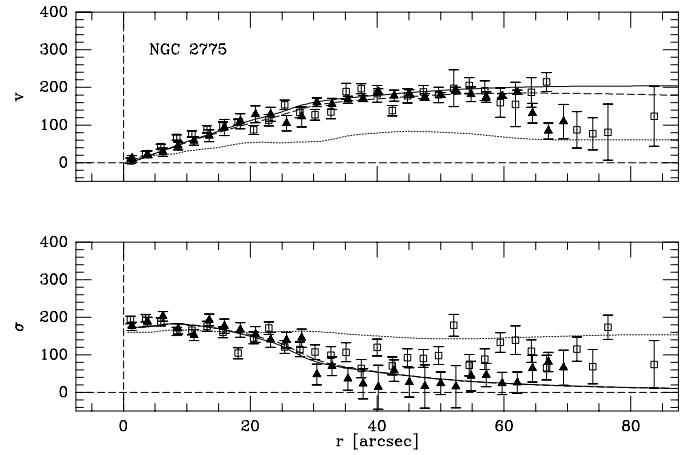


Fig. 12. Same as Fig. 8, but for NGC 2775. The *filled triangles* and the *open squares* represent data derived for the receding SE side and for the approaching NW side respectively. The *dotted line* is the model kinematics for the spheroidal component

mass-to-light ratios of the stellar components in the models with and without the DM halo.

For $|r| > 65''$ the presence on the equatorial plane of the dust ring, which reduces the light contribution of the (faster-rotating) disk stars of a further $\sim 25\%$, causes the observed stellar kinematics to be more affected by the (slower-rotating) bulge stars. In this picture as shown in Fig. 12, our bulge model agrees with the observed drop in velocity and the rise in velocity dispersion. NGC 2775 is a dust-rich system, as can be inferred from its dust-to-HI mass ratio (Roberts et al. 1991), which is ~ 12 times larger than the mean S0/Sa values (Bregman, Hogg & Roberts 1992).

Although the total luminous mass found by Kent (1988) $M_{LM} = 14.3 \cdot 10^{10} M_\odot$ (with $H_0 = 75$ km s $^{-1}$ Mpc $^{-1}$) is in good agreement with ours, his mass decomposition differs from ours. He assumed only the bulge to have an analytical $\mu(r)$ (a de Vaucouleurs law with $\mu_e = 21.0$ mag arcsec $^{-2}$, $r_e = 22''$, $\epsilon_b = 0.12$), while the disk $\mu(r)$ was taken to be the bulge-subtracted major-axis profile. Kent's approach is opposite to ours. We assume the disk to have an analytical $\mu(r)$, and the bulge $\mu(r)$ to be the residual surface brightness after subtracting the disk (assuming no a priori analytical expression or fixed axis ratio). Scaled to our assumed distance, the luminosity of Kent's bulge is $\sim 31\%$ of ours, while our disk luminosity is $\sim 43\%$ of Kent's.

Van der Marel et al. (1991) studied the effects of a $\cos 4\theta$ deviation on the kinematics of NGC 4261. They found that changing the $\cos 4\theta$ Fourier component from zero to ± 0.02 produces variations of $\sim 2\%$ in velocity dispersion and $\leq 10\%$ in rotation velocity. Fig. 13 shows the stellar kinematics of NGC 2775 in the case of slightly disk ($\cos 4\theta = +0.02$) and slightly boxy ($\cos 4\theta = -0.02$) isophotes (solid and dotted line, respectively). The disk model rotates faster and has a lower σ_* than the boxy model in the inner $25''$ (1.9 kpc). The differences in V_* and in σ_* between the two models are < 10 km s $^{-1}$: this means that, in the observed range of values, a difference of 0.04 in $\cos 4\theta$

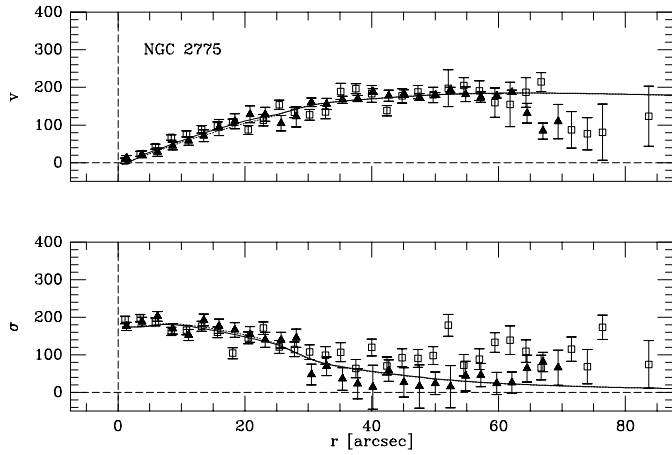


Fig. 13. Predicted stellar kinematics for NGC 2775 with fixed $\cos 4\theta = +0.02$ (solid line) and fixed $\cos 4\theta = -0.02$ (dotted line) at all radii

coefficients corresponds to a difference of $< 12\%$ in velocities and $< 7\%$ in velocity dispersions. However, these uncertainties are immaterial to our results on the mass structure of NGC 2775.

The comparison between V_g and the true circular velocity inferred from the stellar kinematics is shown in the upper panel of Fig. 14. It shows that a DM halo is not strictly required to explain the rotation at large radii ($r \geq 35''$). The contribution of the DM halo to NGC 2775 circular velocity as a function of radius is plotted in the lower panel of Fig. 14. Inside $30''$ on the receding arm, $V_* \simeq V_g$ and $\sigma_* > \sigma_g \simeq 50 \text{ km s}^{-1}$. This rules out the case that the gas kinematics is dominated by random motions, and leads us to speculate that we are looking at gas rotating on a non-equatorial plane. We suggest this is the signature of a past external acquisition (possibly from the companion galaxy NGC 2777) of gas still not completely settled onto the disk plane.

5. Discussion and conclusions

We have presented the ionized-gas and stellar kinematics, measured along the major axis, for a sample of six early-type spiral galaxies. (Due to the high values of σ_g in their inner regions, the gas RCs can not be used as circular-velocity curves.)

For NGC 2179 and NGC 2775, we have modeled both the stellar and the gaseous kinematics to derive the mass contribution of the luminous and dark matter to the total potential, improving on the efforts by Kent (1988) from gas kinematics alone.

We have found that the innermost kinematics ($r < 2R_D$) is very well and uniquely reproduced by taking into account the two luminous components. In the (very luminous) early-type spirals considered here, there is a large inner region in which (essentially) light traces the mass and the DM is a minor mass component. This is agreement with the ‘weak’ maximum disk paradigm proposed by Persic & Salucci (1990), but in disagreement with the claim by Courteau & Rix (1998) according to which in the most luminous spirals DM is a protagonist at essentially any radii.

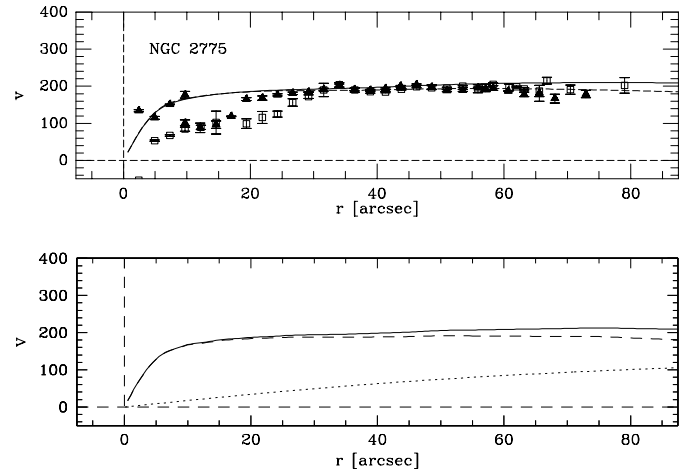


Fig. 14. Same as Fig. 9, but for NGC 2775. The filled triangles and the open squares represent data derived for the receding SE side and for the approaching NW side respectively

More in detail we have found that in NGC 2179 the combined stellar and gaseous rotation data (measured out to about R_{opt}) require the presence of a massive dark halo. In NGC 2775, more luminous and massive than NGC 2179, we can rule out a significant halo contribution out to $0.6 R_{\text{opt}}$. This result complies with the general trend of mass distribution known for later spirals (Persic et al. 1996).

Salucci & Persic (1997), considering a large number of galaxies of mixed morphologies (ellipticals, late spirals, dwarfs, and LSBs), have suggested that the halo structural parameters and the connection between the dark and the luminous matter show a strong continuity when passing from one Hubble Type to another. Ellipticals, considered as luminous spheroids, and spirals, considered as luminous disks, are evidently very different systems, markedly discontinuous in terms of the distribution and global properties of the luminous matter. However, in the structural parameter space, ellipticals and spirals are contiguous, the main difference being that the former are more concentrated in both the dark and luminous components, probably due to the baryons’ dissipational infall being deeper in ellipticals than in spirals (e.g., Bertola et al. 1993). If so, it is hardly surprising that Sa galaxies, being in some sense intermediate systems consisting of a luminous spheroid embedded in a luminous disk, fit in the regularity pattern of the dark-to-visible mass connection shared by ellipticals and spirals. In Fig. 15 we plot our derived dark-to-visible mass ratios at the farthest measured radii for NGC 2179 and NGC 2775 (filled circles) onto the distribution, derived by Salucci & Persic (1997) for galaxies with the same visible mass. The agreement is good. Even if the present result on early-type spirals is preliminary and without pretending to draw general conclusions from one particular case, it nevertheless seems to agree with the idea that, for galaxies of all morphological types, the dark-to-luminous mass ratio at any given radius depends only on the (luminous) mass of the galaxy.

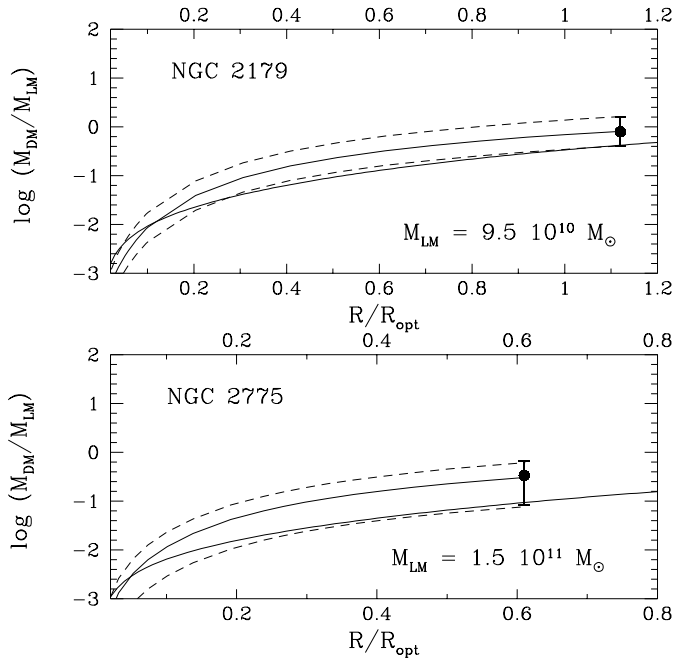


Fig. 15. The dark-to-luminous mass ratio as a function of radius (normalized to R_{opt}) for late spirals of same stellar mass as NGC 2179 and NGC 2775 (solid lines), compared with our derived values for NGC 2179 and NGC 2775 (filled circles)

Acknowledgements. We are indebted to R.P. van der Marel for providing his $f(E, L_z)$ modeling software which became the basis of our modeling package. We also thank R. Falomo for providing some photometric data reduction tools. We are most grateful to the Vatican Observatory Research Group for allocating the observing time. Particular thanks go to R. Boyle, S.J. for his help during the observing run at the VATT. The research of AP was partially supported by an *Acciaierie Beltrame* grant. JCVB acknowledges a grant from Telescopio Nazionale Galileo and Osservatorio Astronomico di Padova. This research has made use of the NASA/IPAC Extragalactic Database (NED) which is operated by the Jet Propulsion Laboratory, California Institute of Technology, under contract with the National Aeronautics and Space Administration.

References

- Bernacca P.L., Perinotto M., 1970, *Contr. Oss. Astr. Asiago* 239, 1
- Bertola F., Rubin V.C., Zeilinger W.W., 1989, *ApJ* 345, L29
- Bertola F., Bettoni D., Rusconi L., Sedmak G., 1984, *AJ* 89, 356
- Bertola F., Pizzella A., Persic M., Salucci P., 1993, *ApJ* 416, L45
- Bertola F., Cinzano P., Corsini E.M., Rix H.-W., Zeilinger W.W., 1995, *ApJ* 448, L13
- Bertola F., Cinzano P., Corsini E.M., et al., 1996, *ApJ* 458, L67
- Bertola F., Cappellari M., Funes J.G., et al., 1998a, *ApJ* 509, L93
- Bertola F., Corsini E.M., Vega Beltrán J.C., et al., 1998b, *ApJ* submitted
- Binney J., Davies R.L., Illingworth G.D., 1990, *ApJ* 361, 78
- Binney J., Tremaine S., 1987, *Galactic Dynamics*. Princeton University Press, Princeton
- Bregman J.N., Hogg D.E., Roberts M.S., 1992, *ApJ* 387, 484
- Cinzano P., 1995, Ph.D. Thesis, Università di Padova
- Cinzano P., van der Marel R.P., 1994, *MNRAS* 270, 325
- Courteau S., Rix H.-W., 1998, *ApJ* in press [astro-ph/9707290]
- de Vaucouleurs, G., de Vaucouleurs A., Corwin H.G. Jr., et al., 1991, *Third Reference Catalogue of Bright Galaxies*. Springer-Verlag, New York (RC3)
- Fasano G., 1990, Internal Report of the Padova Astronomical Observatory
- Fillmore J.A., Boroson T.A., Dressler A., 1986, *ApJ* 302, 208
- Freeman K.C., 1970, *ApJ* 160, 811
- Gerhard O.E., 1993, *MNRAS* 265, 213
- Gerhard O.E., Vietri M., Kent S.M., 1989, *ApJ* 345, L33
- Hernquist L., 1990, *ApJ* 356, 359
- Hoffleit D., Jaschek C., 1982, *The Bright Star Catalogue*. Yale University Observatory, New Haven (BSC)
- Keel W.C., 1996, *ApJS* 106, 27
- Kent S.M., 1985, *ApJS* 59, 115
- Kent S.M., 1988, *AJ* 96, 514
- Kormendy J., Westpfahl D.J., 1989, *ApJ* 338, 752
- Jaffe W., 1983, *MNRAS* 202, 995
- Lauberts A., Valentijn E.A., 1989, *The Surface Photometry Catalogue of the ESO-Uppsala Galaxies*. ESO, Garching bei München
- Osterbrock D.E., Fulbright J.P., Martel A.R., Keane M.J., Trager S.C., 1996, *PASP* 108, 277
- Peletier R.F., Davies R.L., Illingworth G.D., Davis L.E., Cawson M., 1990, *AJ* 100, 1091
- Persic M., Salucci P., 1990, *MNRAS* 247, 349
- Persic M., Salucci P., Stel F., 1996, *MNRAS* 281, 27
- Roberts M.S., Hogg D.E., Bregman J.N., Forman W.R., Jones C., 1991, *ApJS* 75, 751
- Rood H.J., Page T.L., Kintner E.C., King I.R., 1972, *ApJ* 175, 627
- Rubin V.C., Burstein D., Ford W.K. Jr., Thonnard N., 1985, *ApJ* 289, 81
- Salucci P., Persic M., 1997, In: Persic M., Salucci P. (eds.) *ASP Conf. Ser. 117, Dark and Visible Matter in Galaxies and Cosmological Implications*. ASP, San Francisco, p. 1
- Sandage A., Bedke J., 1994, *The Carnegie Atlas of Galaxies*. Carnegie Institution, Flintridge Foundation, Washington (CAG)
- Sandage A., Tammann G.A., 1981, *A Revised Shapley-Ames Catalog of Bright Galaxies*. Carnegie Institution, Washington (RSA)
- Sargent W.L.W., Schechter P.L., Boksenberg A., Shortridge K., 1977, *ApJ* 212, 326
- Sato C., 1980, *PASJ* 32, 41
- Tully R.B., 1988, *Nearby Galaxies Catalog*. Cambridge University Press, Cambridge
- van der Marel R.P., 1991, *MNRAS* 253, 710
- van der Marel R.P., Binney J., Davies R.L., 1990, *MNRAS* 245, 582
- van der Marel R.P., Franx M., 1993, *ApJ* 407, 525
- Wilson R.E., 1953, *General Catalogue of Stellar Radial Velocities*. Carnegie Institution, Washington